

A mathematical model of the metabolic and perfusion effects on cortical spreading depression

Joshua C. Chang^{1*}, K.C. Brennan², Dongdong He³, Huaxiong Huang⁴, Robert M. Miura⁵, Phillip L. Wilson⁶, Jonathan J. Wylie⁷

1 Department of Biomathematics, University of California, Los Angeles, USA.

joshchang@ucla.edu

2 Department of Neurology, University of Utah, Salt Lake City, Utah, USA.

k.c.brennan@hsc.utah.edu

3 Department of Mathematics and Statistics, York University, Toronto, Ontario, Canada

M3J 1P3. ddonghe@yorku.ca

4 Department of Mathematics and Statistics, York University, Toronto, Ontario, Canada

M3J 1P3. hhuang@yorku.ca

5 Department of Mathematical Sciences and Center for Applied Mathematics and

Statistics, New Jersey Institute of Technology, Newark, NJ 07102 USA. miura@njit.edu

6 Department of Mathematics and Statistics, University of Canterbury, Christchurch,

New Zealand. p.wilson@math.canterbury.ac.nz

7 Department of Mathematics, City University of Hong Kong, Kowloon Tong, Hong

Kong. mawylie@cityu.edu.hk

*** E-mail: joshchang@ucla.edu**

Abstract

Cortical spreading depression (CSD) is a slow-moving ionic and metabolic disturbance that propagates in cortical brain tissue. In addition to massive cellular depolarization, CSD also involves significant changes in perfusion and metabolism – aspects of CSD that had not been modeled and are important clinically. In this study, we develop a mathematical model for CSD where the sodium-potassium-ATPase, responsible for neuronal polarization and recovery from CSD, operates at a rate that is dependent on the supply of oxygen. The supply of oxygen is determined by modeling blood flow through a lumped vascular tree with an effective local vessel radius that is controlled by the extracellular potassium concentration. Our model replicates the qualitative and quantitative behavior of CSD found in experimental studies and elucidates the effect of oxygen deprivation on CSD recovery. We show that during CSD, the metabolic activity of the cortex outstrips the physiological limits placed on oxygen delivery, regardless of vascular constriction or dilation. However, vasoconstriction and vasodilation play important roles in determining the susceptibility of the cortical tissue to CSD and its recovery. Our study incorporates relevant perfusion and metabolic factors into a model of CSD, and in doing so, helps explain the varied phenotypes of this phenomenon *in vitro* and *in vivo*.

Author Summary

Cortical Spreading Depression (CSD) is a traveling wave of electrical disturbance in the brain that is associated with migraine and brain injury. Massive changes in cerebral blood flow have been associated with CSD, but thus far no mathematical modeling has incorporated these physiologically important changes. In this manuscript, we present a mathematical model for CSD that incorporates blood flow and oxygen consumption in order to examine the effects of the brain vasculature on CSD and vice versa.

1 Introduction

Cortical spreading depression (CSD) is a propagated depolarization that occurs in the gray matter of many species [1]. In humans, it is known to occur during brain injury, stroke, and subarachnoid hemorrhage [2]. There is also strong evidence that CSD is responsible for migraine aura [3–5].

Although CSD was discovered in 1944 by Leão [6], we still do not have a detailed understanding of how CSD is manifest. In particular, CSD has been associated with massive changes in cortical perfusion. The magnitudes of these changes vary by animal species, but significant decreases and increases in blood flow or volume occur in all species tested [7–9]. Also common to all species tested is a mismatch in the delivery of substrates to meet metabolic demands, i.e., a derangement of neurovascular coupling [10, 11].

Blood delivery is known to play a significant role in CSD in several ways. Changes in perfusion can induce CSD during stroke, called a peri-infarct depolarizations (PID). Conditions that mimic the effects of hypoperfusion, such as oxygen glucose deprivation (OGD) and exposure to ouabain (an inhibitor of the sodium potassium ATPase), also generate spreading depolarizations [12–14].

Perfusion changes can also modulate the signature characteristics of CSD. Depending on the levels of the underlying oxygenation or blood pressure, the amplitude and duration of depolarization and the velocity of propagation of CSD can be altered [14, 15]. Clearly, CSD in vivo cannot be understood without reference to the vascular changes that condition - and are conditioned by - the phenomenon. There is a need to further explore the implications of the effects of perfusion and metabolism on various aspects of CSD.

Such explorations naturally lead to the development of mathematical models in which many mechanisms can be studied independently and/or simultaneously. Mathematical models of CSD have accounted for ionic diffusion, cellular membrane ionic currents, sodium-potassium-ATPase, and extra- and intracellular volume changes. Thus far, mathematical models of CSD have not looked at the dynamical implications of neurovascular coupling and metabolism. Here we develop a mathematical model that uses known physiological data relating effective blood vessel diameter and extracellular potassium concentration to model oxygen delivery in the brain. We show that the oxygen deprivation that results from both metabolic demand and vasoconstriction modifies the characteristics of CSD waves and helps explain some of the variability of CSD between species and even within the same animal. Our model also explains differences between CSD in vivo and CSD in brain slices.

Previous mathematical models of CSD have accounted for extracellular space and intracellular space (both somatic and glial). Here, we formulate a five-compartment continuum model for CSD (neurons consisting of two compartments, extracellular space consisting of two compartments, and vascular tree compartment), and perform numerical tests of the model under various conditions. A glial compartment is not considered in this model except in the context of potassium buffering. Finally, we discuss the results of simulations of the model and its relevant clinical and translational implications.

2 Model

To study the important new elements that affect and are affected by CSD, we formulate a five-compartment continuum model. Neurons comprise two of the five compartments: a compartment representing the dendritic processes (d), and a compartment representing the cell bodies (somatic compartment s). The extracellular space (e) also comprises two of the compartments, with the extracellular space proximal to cell bodies and proximal to dendrites each receiving a compartment. The vascular bed (v) comprises the remaining compartment. For computational tractability, we make the simplifying assumptions that were made in Yao et al. [16], that the intra- and extracellular volume fractions remain fixed.

The neuronal and extracellular compartments include only the most-relevant ions (sodium, potassium, chloride) and channels that have been shown to be the most responsible for the instigation and spread of CSD [16–18]. In the somatic membranes, we include T-type sodium channels, P-type sodium channels,

delayed-rectifier potassium channels, A-type potassium channels, and the sodium-potassium ATPase. In the dendritic membranes, we additionally include NMDA channels.

Our model assumes that the vascular compartment does not exchange fluid with the extracellular space, so that it does not affect the intra- and extracellular volume fractions. The effective diameters of proximal arterioles controls the blood flow rate. In turn, the vascular diameters are coupled to neuronal activity through extracellular potassium concentrations proximal to dendritic processes.

2.1 Membrane potential and ion transport using a neuronal model

The membrane potentials of the neuronal compartments $E_{m,*}$ (* is either s for somatic or d for dendritic), are governed by the coupled ordinary differential equations

$$C_m \frac{dE_{m,s}}{dt} = -I_{s,\text{tot}} + \overbrace{\frac{1}{2R_a\delta_d^2} (E_{m,d} - E_{m,s})}^{\text{dendrite coupling}} \quad (1)$$

$$C_m \frac{dE_{m,d}}{dt} = -I_{d,\text{tot}} + \overbrace{\frac{1}{2R_a\delta_d^2} (E_{m,s} - E_{m,d})}^{\text{soma coupling}} \quad (2)$$

where C_m is the membrane capacitance per unit surface area ($\mu\text{farad}/\text{cm}^2$) for both the somatic and dendritic membranes, R_a is the input resistance of the effective dendritic tree, δ_d is the half length of the effective dendritic tree, and $I_{*,\text{tot}} = \sum_{\text{ions}} I_{*,\text{ion,tot}} = \sum_{\text{ions}} \sum_{\text{channels}} I_{*,\text{ion,channel}}$ are the spatially-dependent total cross-membrane ionic currents per unit surface area (mA/cm^2) for each neuronal compartment. Following Kager et al. [17,18] and Yao et al. [16], the total cross-membrane currents, $I_{*,\text{tot}}$, are given for the three major ions (sodium, potassium, and chloride) and are the sum of the active and passive (leak) sodium and potassium currents, the chloride (leak) current, and the sodium-potassium exchange pump current (see Appendix A).

The local rates of change of the extracellular ions (Na^+ , K^+ , and Cl^-) are due to membrane ionic currents, diffusion of extracellular ions both within and between the extracellular compartments, and the buffering of extracellular potassium. They are given by

$$\begin{aligned} \frac{\partial([\text{ion}]_{e,s})}{\partial t} &= \overbrace{\frac{S_s}{f_e F V_s} I_{s,\text{ion,tot}}}^{\text{through channels}} \\ &+ \overbrace{\frac{\partial}{\partial x} \left(D_{\text{ion}} \frac{\partial[\text{ion}]_{e,s}}{\partial x} \right)}^{\text{diffusion within compartment}} \\ &+ \overbrace{\frac{D_{\text{ion}}(V_d + V_s)}{2\delta_d^2 V_s} ([\text{ion}]_{e,d} - [\text{ion}]_{e,s})}^{\text{exchange with dendritic extracellular space}} \end{aligned} \quad (3)$$

$$\begin{aligned} \frac{\partial([\text{ion}]_{e,d})}{\partial t} &= \frac{S_d}{f_e F V_d} I_{d,\text{ion,tot}} \\ &+ \frac{\partial}{\partial x} \left(D_{\text{ion}} \frac{\partial[\text{ion}]_{e,d}}{\partial x} \right) \\ &+ \frac{D_{\text{ion}}(V_s + V_d)}{2\delta_d^2 V_d} ([\text{ion}]_{e,s} - [\text{ion}]_{e,d}) \end{aligned} \quad (4)$$

where $S_{(*)}$ are the surface areas of the neuronal compartments in the total fixed volume given by the sum of the fixed somatic V_s , dendritic V_d , extracellular somatic $f_e V_s$, and extracellular dendritic $f_e V_d$ volumes. The equations for extracellular potassium are modified by adding the buffering flux given in Section 2.3. The equations for the rates of change of intracellular ions are

$$\frac{d([\text{ion}]_{i,s})}{dt} = \underbrace{-\frac{S}{FV_s} I_{s,\text{ion,tot}}}_{\text{through channels}} + \underbrace{\frac{D_{\text{ion}}(V_d + V_s)}{2\delta_d^2 V_s} ([\text{ion}]_{i,d} - [\text{ion}]_{i,s})}_{\text{exchange with dendrites}} \quad (5)$$

$$\frac{d([\text{ion}]_{i,d})}{dt} = -\frac{S}{FV_d} I_{d,\text{ion,tot}} + \frac{D_{\text{ion}}(V_s + V_d)}{2\delta_d^2 V_d} ([\text{ion}]_{i,s} - [\text{ion}]_{i,d}). \quad (6)$$

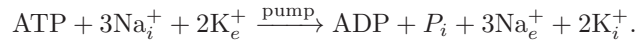
Note that we have not included the diffusion of intracellular ions because any appreciable diffusion (relative to cell size) that would require the ions to first become an extracellular ion and then diffuse extracellularly.

As Cl^- is the only extracellular anion in our simulations, to ensure electroneutrality, its initial extracellular concentrations $([\text{Cl}^-]_{e,*})$ were determined by the sum of the concentrations of the major cations: $[\text{Cl}^-]_{e,*} = [\text{Na}^+]_{e,*} + [\text{K}^+]_{e,*}$. We chose the initial intracellular concentrations of chloride $([\text{Cl}^-]_{i,*})$ so that its Nernst potentials matched the membrane potentials. For electroneutrality intracellularly in the soma and dendrites, we added a non-specific immobile anion. Although calcium can have major effects on neurotransmitter dynamics and other secondary messenger effects, we ignored the calcium concentration because of its relatively small values.

2.2 Exchange pumps

During CSD, the ionic concentrations in the extra- and intracellular spaces are considerably displaced from steady-state. This displacement occurs primarily because of fluxes through voltage-gated sodium and potassium channels. Here, we include the sodium-potassium exchange pumps (Na-K-ATPase) in the neuronal membranes, whose primary role is to restore the ionic concentrations back to their homeostatic state. The ionic pumps are active and consume energy. When local oxygen levels are depleted, ATP is in short supply. Therefore, the function of the ionic pumps is related in our model to oxygen consumption and vascular flows.

These pumps are involved in the movements of intracellular sodium and extracellular potassium against their electrochemical gradients require active ionic pumps that consume energy and the pumps are fueled by the dephosphorylation of ATP in the cell [19] given by



When local oxygen in the tissue is very low, the normal ATP dynamics are perturbed.

The Na^+/K^+ -ATPase is a trans-membrane protein with two extracellular binding sites for potassium, three intracellular binding sites for sodium, and a single intracellular binding site for ATP. In each neuronal compartment, its potassium and sodium currents are given by $I_{*,\text{K,pump}} = -2I_{*,\text{pump}}$ and $I_{*,\text{Na,pump}} = 3I_{*,\text{pump}}$, respectively, where

$$I_{*,\text{pump}} = I_{\text{max}} \gamma_{*,\text{pump},1} \gamma_{*,\text{pump},2}$$

and

$$\begin{aligned} \gamma_{*,\text{pump},1}([\text{K}^+]_{e,*}, [\text{Na}^+]_{i,*}) \\ = \left(1 + \frac{[\text{K}^+]_{e,0}}{[\text{K}^+]_{e,*}}\right)^{-2} \left(1 + \frac{[\text{Na}^+]_{i,0}}{[\text{Na}^+]_{i,*}}\right)^{-3}. \end{aligned} \quad (7)$$

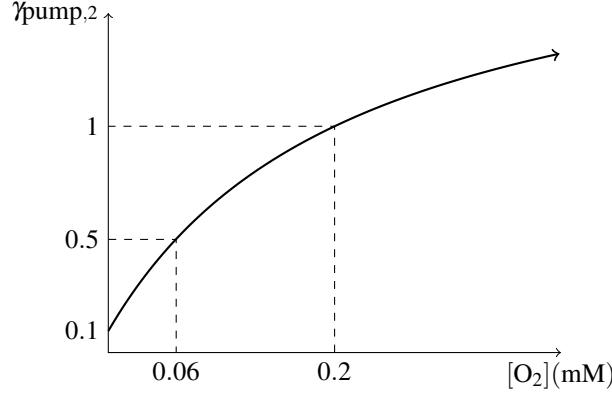


Figure 1. Oxygen availability affects the Na^+/K^+ -ATPase. Shown is the relationship between tissue oxygen concentration and the oxygen-dependent portion of the pump rate (Eq 8). Since some ATP is generated even in the absence of oxygen, the pump rate does not completely go to zero as the oxygen concentration approaches zero. The steady state oxygen concentration is 0.2mM.

This expression is given in [17] and is a Hill equation for the pump rate under the assumption of plentiful ATP. We modify this equation so that it is valid even in the low-ATP regime by including another Hill-like term of the form $(1 + [\text{ATP}]_0/[\text{ATP}])^{-1}$. The Hill-exponent is set to 1 to obey the known stoichiometric rule for the pump.

To use this formulation for the pump activity, one needs to understand ATP dynamics within the cell. Cloutier et al. [20] provides a detailed system of ordinary differential equations for the generation of ATP through both aerobic and anaerobic respiration. One of their key assumptions is that adenylate kinase is in quasi-static equilibrium. This assumption is invalid for situations where the system is under high metabolic stress. Instead, we assume that production and consumption of ATP are dominant, thereby finding a quasi-steady-state relationship between ATP and O_2 , $\text{ATP} = \text{const}_1 + \text{const}_2 \left(\frac{\text{O}_2}{\text{const}_3 + \text{O}_2} \right)$.

Thus, we can describe the pump rate explicitly in terms of oxygen availability with the expression

$$\gamma_{\text{pump},2}([\text{O}_2]) = 2 \left(1 + \frac{[\text{O}_2]_0}{(1 - \alpha)[\text{O}_2] + \alpha[\text{O}_2]_0} \right)^{-1} \quad (8)$$

where α is the percentage (about 5%) of ATP production that is independent of oxygen [21, 22], the subscript 0 denotes the equilibrium values, and $[\text{O}_2]$ is the tissue oxygen concentration (see Fig 1). This expression indicates that the pumping rate will be reduced whenever there is a decrease of the oxygen level in the tissue.

2.3 Potassium buffering

Astrocytes play important roles in the instigation and propagation of CSD and in the neurovascular coupling through neurotransmitter-mediated signaling pathways [23]. A principal role of astrocytes is to buffer extracellular potassium [24]. This buffering is achieved through a variety of inward rectifying potassium channels in the glial membrane and is bolstered by the extreme polarity of glial cell membranes with membrane potential near the Nernst potential for potassium. For this study, we are not interested in the exact mechanisms of glial potassium buffering, but are interested in reproducing accurate potassium dynamics for our model. Thus, we incorporate astrocyte effects through empirical potassium buffering.

Following Kager et al. [17], we modeled the potassium-buffering flux, v_{buffer} , by the following first-order ordinary differential equation, valid at each position in the extracellular continuum

$$v_{\text{buffer}} = -\frac{dB}{dt} = \mu_+[K^+]_e B \exp\left(\frac{[K^+]_e - 5.5}{-1.09}\right) - \mu_-(B_0 - B), \quad (9)$$

where B (mM) is the free extracellular buffer concentration, the rate constants $\mu_+ = \mu_- = 8.0 \times 10^{-6} \text{ms}^{-1}$ determine the speed at which potassium is buffered, and $B_0 = 200$ mM is the effective total buffer concentration. This equation describes strong buffering of extracellular potassium for concentrations above 5.5 mM, but is limited by saturation of the finite buffer. As the amount of buffered potassium increases, re-release of potassium into the extracellular space becomes more favorable. The initial value of the free buffer concentration is set to maintain steady state when the extracellular potassium concentration is at its rest value (3.5 mM).

2.4 Neurovascular coupling and oxygen supply

We now describe how the tissue oxygen level is affected by and influences CSD. First, we assume that there exists an effective blood vessel radius r and that the cerebral blood flow rate (CBF) is given by

$$\text{CBF} = \text{CBF}_0 \frac{r^4}{r_0^4} \quad (10)$$

in which the equilibrium values are again denoted by the subscript 0. This expression is based on the empirical observation that blood flow through the small vessels where nutrient exchange primarily occurs can be modeled as Poiseuille flow where the volume flow rate is proportional to r^4 [25].

We use an empirical model for the effective vessel radius r , based on replicating the activity observed in many experimental studies on the subject [26, 27]. Extracellular potassium is known to dilate vessels at lower concentration elevations (less than ~ 17 mM), and constrict vessels at higher concentration levels [28]. To reproduce this behavior, we assume that the effective vessel radius is given by

$$r([K^+]_e) = r_0 \exp \left\{ \overbrace{-\left(\frac{[K^+]_e - 3.5}{a}\right)^2}^{\text{constriction}} \right\} \times \frac{\overbrace{\left(1 + be^{-[(K^+]_e - 10)/c}\right)^2}^{\text{dilation}}}{1 + be^{-(6.5/c)^2}}, \quad (11)$$

which is a product of constricting and dilating terms. Since dendrites are long neuronal processes that occupy a greater volume than cell bodies, we take $[K^+]_e$ to be the concentration in the dendritic extracellular space. The parameter a (mM) controls the constriction response, b controls the amount of maximal dilation in the vessel, and c (mM) controls the dilation response. We found values of $a = 50$ mM, $b = 0.18$, $c = 3$ mM to mimic the vascular response of Farr and David [28] (see Fig 2), who provide a model for the radius of cerebral arterioles based upon currents through potassium channels in the membranes of vascular cells. Using this expression gives us a simple relationship between the extracellular potassium

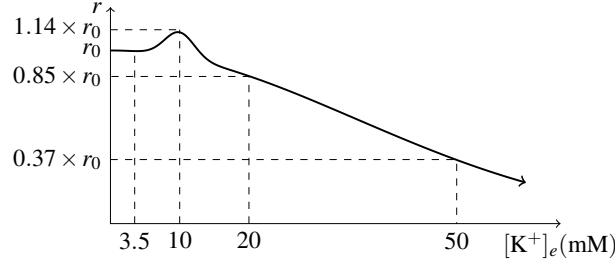


Figure 2. Relationship between vascular caliber and $[K^+]_e$ Effective vascular radius r as a function of extracellular potassium concentration $[K^+]_e$.

concentration and CBF, namely,

$$\begin{aligned} \text{CBF} = \text{CBF}_0 & \left[\exp \left\{ - \left(\frac{[K^+]_e - 3.5\text{mM}}{a} \right)^2 \right\} \right]^4 \\ & \times \left[\frac{\left(1 + b e^{-([K^+]_e - 10\text{mM})/c} \right)^2}{1 + b e^{-(6.5\text{mM}/c)^2}} \right]^4. \end{aligned} \quad (12)$$

We model the temporal evolution of the tissue oxygen concentration $[O_2]$, using a reaction-diffusion equation

$$\frac{\partial [O_2]}{\partial t} = D_{O_2} \frac{\partial^2 [O_2]}{\partial x^2} + S$$

with nonlinear source term given by

$$\begin{aligned} S = \text{CBF} & \frac{[O_2]_b - [O_2]}{[O_2]_b - [O_2]_0} \\ & - \text{CBF}_0 \frac{\gamma_{\text{pump},2}([O_2]) - \gamma_{\text{pump},2}(0)}{\gamma_{\text{pump},2}([O_2]_0) - \gamma_{\text{pump},2}(0)} \left((1 - \gamma) \right. \\ & \left. + \gamma \frac{\gamma_{s,\text{pump},1}([K^+]_{e,s}, [Na^+]_{i,s}) + \gamma_{d,\text{pump},1}([K^+]_{e,d}, [Na^+]_{i,d})}{2\gamma_{\text{pump},1}([K^+]_{e,0}, [Na^+]_{i,0})} \right). \end{aligned} \quad (13)$$

The first term in the source is the amount of oxygen transferred from the blood stream to the tissue and is given by the product of CBF and the normalized concentration difference in oxygen tension between the blood and the tissue. The remaining terms represent the consumption of oxygen by the sodium-potassium exchange pump and other cellular processes that are assumed to remain steady during CSD. The pump consumption is given by the product of the equilibrium CBF and pump rate normalized by the steady-state pump rate. A fraction $0 < \gamma < 1$ of the total oxygen consumption at steady-state is due to the pump. Experimental estimates of this parameter have ranged from as low as 0.10 [29] to as high as 0.70 [30]. We include simulations over the full spectrum for thoroughness. Note that we have $S = 0$ at steady-state.

3 Numerical Tests

In order to shorten numerical computational time, we sought to reduce the size of the computational domain to the minimal size required in order to achieve stable propagating waves that did not exhibit

boundary effects. In order to do this, we used a minimal amount of potassium to induce CSD. We found that for injections of Gaussian boluses with 120 micron width, a K^+ concentration of 15mM was sufficient to induce CSD. This concentration is near the experimentally-determined minimum threshold for CSD induction [31], and confirmed to us that our phenomenological potassium buffer was behaving in a physiologically realistic manner.

We performed one-dimensional simulations by breaking up our model into a system of ODEs solved using Matlab routine `ode15s`, with reflecting boundary conditions. The computational domain was set to a length of 2.7 cm, and discretized into 46 grid points. This domain was sufficiently long for the propagating wave to become stable and for boundary effects to remain insignificant. For diffusion, we used a centered finite-difference approximation of the Laplacian operator, resulting in a system of ordinary differential equations for the ionic and oxygen concentrations at each grid point. We measured the duration of potassium elevation by taking the total amount of time that $[K^+]_{e,d}$ is above 6 mM. The transient sodium channel had negligible effect on the ionic currents during CSD (data not shown), so we chose to omit it from these simulations.

The variables in the dendritic and somatic compartments did not differ significantly in any of the simulations. For this reason, we report results from the dendritic compartments and drop the corresponding prefix.

3.1 Oxygen-clamped simulations

First, we simulated our model with the oxygen coupling completely turned off, i.e., $\gamma = 0$ (see Eq 13). Thus, the sodium-potassium-ATPase does not consume any oxygen, and we assume that the tissue oxygenation is held at its steady state value. In this situation, we obtain CSD waves with a velocity of 3.2 millimeters per minute and with extracellular potassium concentration increasing to a maximum value of 45.7 mM. The total duration of the elevated extracellular potassium concentration is 65.4 seconds (Fig 3).

The potassium buffer acts similar in that in Kager et al. [17]. It saturates rapidly, after which it is responsible for a net re-release of potassium into the extracellular environment. The buffer acts this way in all simulations as it is independent of the oxygen level in our model. For this reason, we omit further mention of the potassium buffer.

3.2 Blood vessel-clamped simulations

Next, we simulated CSD where the effective blood vessel diameter remained fixed, thereby fixing the maximal oxygen flux rate into the tissue. We varied the oxygen coupling parameter γ between 0 (no oxygen consumption by pump) and 1 (maximal oxygen coupling) in increments of 0.025.

The results, shown in Fig 4, illustrate the response of CSD to oxygen coupling. By increasing γ , we increase the duration and the amplitude of the CSD waveform. To get a deeper understanding of these results, Fig 5 shows the macroscopic observables. One sees that increases in γ lead to greater drops in oxygenation. This deoxygenation results in decreases in the magnitude of the sodium-potassium-ATPase pump current, resulting in longer tails of recovery for both membrane potential and extracellular potassium concentration.

3.3 Coupled vasculature

From the previous results, one sees that oxygenation has a definite impact on susceptibility of the tissue to CSD and on its recovery. The next question is whether vasoconstriction has an impact on CSD. We performed a series of simulations where we activated the vascular coupling that we defined in Eqs. 11 and 13. We simulated an idealized vascular response, using parameters mimicking the vascular behavior

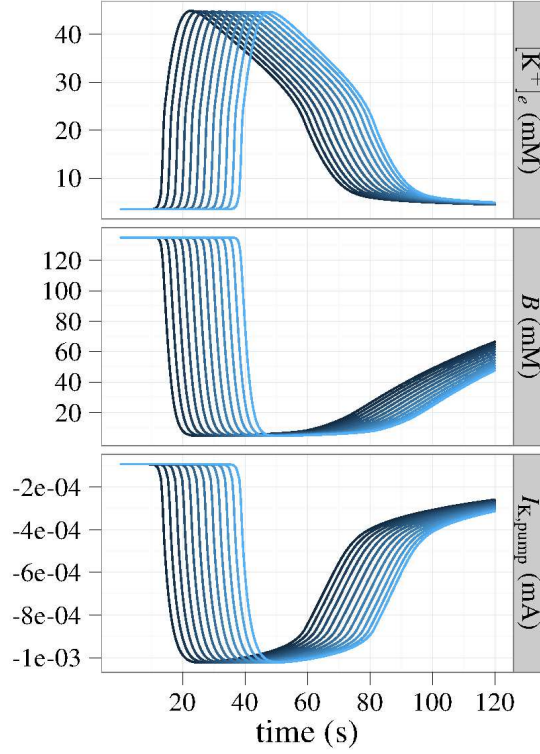


Figure 3. CSD in absence of oxygen consumption. Shown are the time-courses of the propagating waves of extracellular potassium concentration, free buffer capacity, membrane potential, and sodium-potassium-ATPase pump rate at positions 120 microns apart for simulations performed in the absence of oxygen consumption by the Na^+/K^+ -ATPase. The Na^+/K^+ -ATPase operates at rates determined solely by $[\text{K}^+]_e$ and $[\text{Na}^+]_i$.

of Farr and David [28]. In these simulations, we varied the oxygen coupling parameter, γ , in order to see the variability in behavior one might expect to see in an idealized CSD experiment.

The results, shown in Fig 6, illustrate the effects of vascular coupling. One can see that the effective blood vessel radius drops rapidly to approximately 40% of its original value. The drop leads to steep sustained reductions in the oxygen concentration during the metabolic challenge of the CSD wave. The deoxygenation is reflected in the pump rate, where a large increase of inward potassium current at the beginning of CSD is rapidly diminished as oxygen is depleted. The implications of this chain of events are visible in the extracellular potassium profile.

As we noted earlier, vascular response is variable, depending on factors such species, individual, and metabolic states. In Fig 8, the effects of this variability are seen in simulations across a grid of values for the parameters a, b, γ (Eq. 11). The duration of the CSD event decreases as the constriction parameter a is increased, and as the dilation parameter b is increased.

In Fig 9, we have plotted the speed of CSD waves across the spectrum of possible vascular responses. These vascular responses are parameterized mainly by two parameters, the constriction parameter a , and the dilation parameter b (Eq. 11).

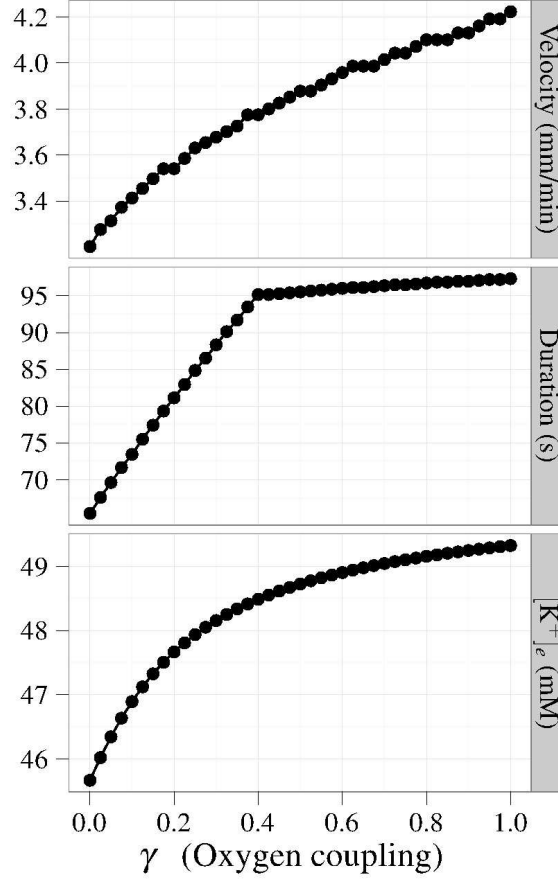


Figure 4. Oxygen coupled to Na^+/K^+ ATPase. Fixing the effective vascular radius while coupling oxygen to the sodium-potassium-ATPase gives a purely consumption-based view of oxygen during CSD. Defining coupling as the fraction of oxygen consumed by the pump at steady-state, these simulations show that all of the CSD characteristics – speed, duration, maximum $[\text{K}^+]_e$ – increase with an increase in the coupling constant γ . The duration of the wave increases linearly from $\gamma = 0$ to $\gamma \approx 0.4$ before increasing linearly at a different rate when $\gamma > 0.4$.

4 Discussion of major findings

Since its discovery, CSD has been known to involve massive changes in vascular caliber, and hence, perfusion [6]. Up to this point, these changes, which can have profound effects on cortical function and thus on CSD itself, have not been incorporated into CSD models. Using our model, we were able to examine the effects of vascular activity on CSD.

4.1 Relationship between vascular activity and CSD

Integration of different vascular effects more closely approximates in vivo CSD and helps explain why CSD seems to be different in slice preparations. Our numerical experiments confirmed that oxygen delivery

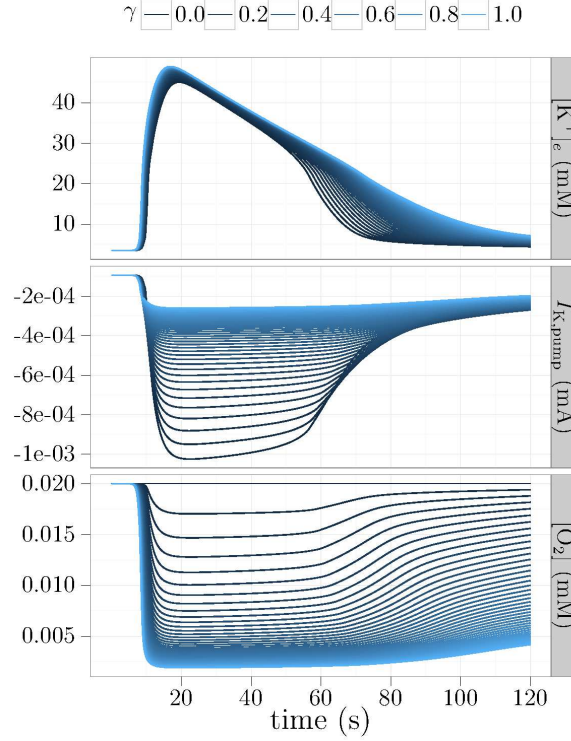


Figure 5. Fixed vascular caliber. Time courses at a fixed position, $780\mu\text{m}$ downstream of the original stimulus. These simulations show the effects of oxygen consumption on CSD for a range of the oxygen coupling parameters, γ . Increasing γ prolongs the duration and magnifies the amplitude of the CSD because it implies that the pump consumes more of the available oxygen, thereby resulting in larger oxygen depletions.

plays a significant role in the dynamics of CSD. Even in the absence of constriction, oxygen depletion is seen. This fact, however, did not absolve the constriction from its implication in oxygen depletion. Additionally, vasoconstriction and vasodilation were seen to further modify the characteristics of the CSD wave, particularly in the low- γ regime.

By varying the relationship between vasoconstriction and extracellular potassium, we achieved a continuum of CSD responses that could explain real physiological variability across species, within members of the same species, and across repeated CSDs in the same animal.

4.1.1 CSD uncoupled from vascular activity

Our modeling of CSD uncoupled from oxygen concentration resembles current CSD models, which rely on similar assumptions and conductances. Such models are relevant to CSD in ex-vivo brain slices, where the perfusing medium has contact with an essentially unlimited source of oxygen. In this case, the pump is always able to perform at a rate determined by $[\text{K}^+]_e$ and $[\text{Na}^+]_i$, and the total pump current is constrained only by the total number of available pumps present, provided that there is sufficient nutrient available.

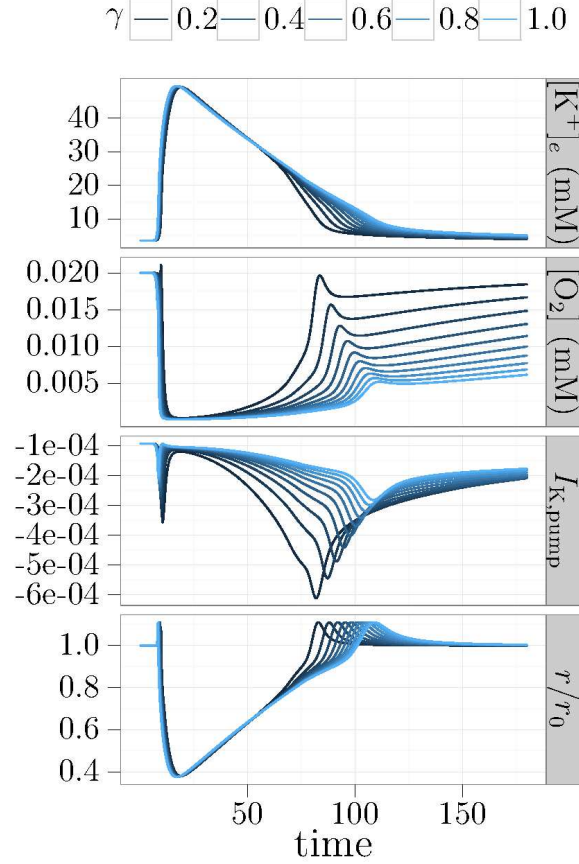


Figure 6. “Typical” vascular coupling. Time courses at a fixed position, $780\mu\text{m}$ downstream of the original stimulus. Simulations performed using vessel of Farr and David [28]. After a short dilation period, the vessels constrict significantly to about 40% of their rest radii, before recovering.

4.1.2 CSD coupled with vascular activity

Coupling an inert vasculature into CSD, one obtains a sense of the metabolic demands that CSD places on the cortex. The large displacements of sodium and potassium require the use of energy to rectify, and the physical constraints placed on blood delivery by the physiologically reasonable assumption of finite volume-flow-rate were seen to result in depletion of oxygen and reduction in potassium flux through the pumps. This finding is consistent with in vivo measurements of tissue oxygen and mitochondrial redox state – even with mild dilation. Several studies have found that both variables moved into a more-reduced oxidative state [32,33]. In our model, the depletion of oxygen is due to increased metabolic demand driven by the sodium-potassium-ATPase.

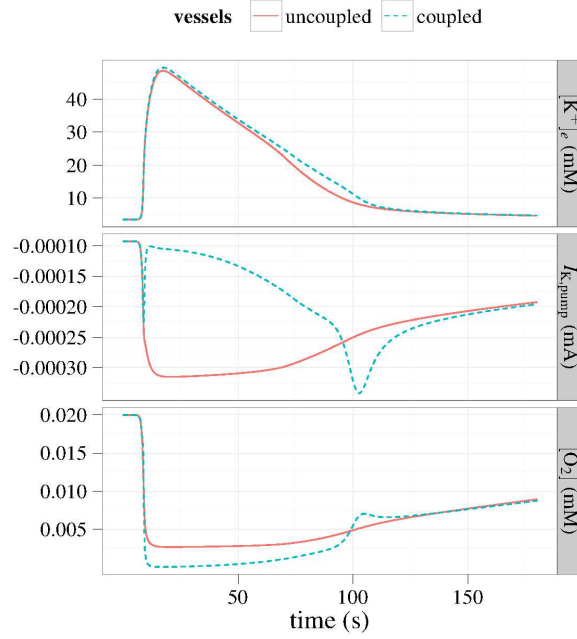


Figure 7. Effect of vascular coupling. When vasculature is coupled to $[K^+]_e$, the extra depletion of oxygen due to supply constraints causes the pump to operate at a slower rate than when vasoconstriction does not occur. As a consequence, the inward potassium flux through the pump is decreased. The result is prolonged recovery time. Shown are simulations where $\gamma = 0.7$.

4.1.3 The effects of vasoconstriction/vasodilation

Furthermore, we show that vasoconstriction can both increase tissue's susceptibility to CSD and impair its ability to recover. These effects are due to the reductions in blood flow causing a significant additional drop in cortical oxygenation levels. In Fig 6, the vessel is seen to constrict to approximately 40% its original radius. This constriction is within the experimental range reported in Chang et al. [10]. Due to the power-law relationship between blood flow and effective blood vessel radius, even a small reduction in effective radius has large blood flow implications. A 60% constriction results in blood flow dropping to 2.6% of its original value. This effect is visible in the oxygenation level, which undergoes further decreases. Our simulations show that both wave speed and recovery time increase when vessel constriction is greater.

Our simulations also show that vasodilation plays a role in CSD. Predictably, vasodilation appears to precondition the tissue so that it is more able to withstand the increase of extracellular K^+ that accompanies the CSD wave. Due to the power law relationship, an increase of 14% in the vessel radius results in a 70% increase in blood volume flow rate. The result shown in Fig 9 is a tissue that is more able to withstand potassium elevations, thereby causing slow-downs in the CSD wave. Vasodilation (beyond the effective resting radius) seems to play a significant role in the recovery from CSD, causing decreases in the recovery time (Fig 8).

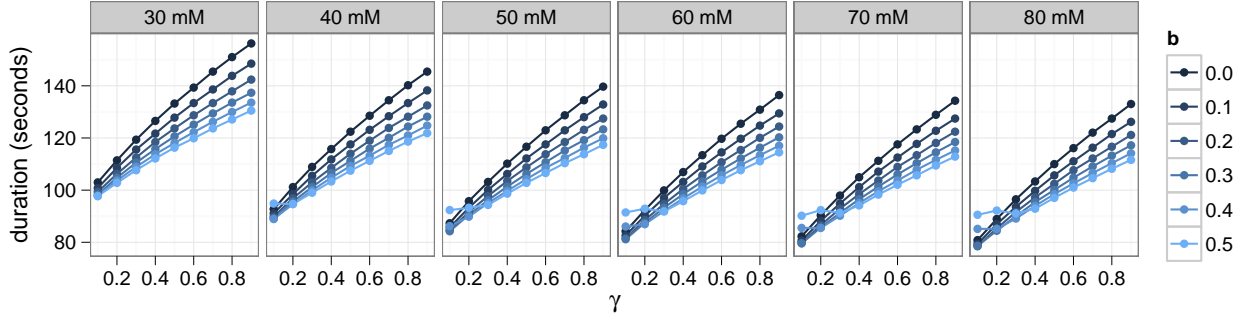


Figure 8. Duration of CSD for different vascular responses. Shown are CSD durations plotted against percent dilation b (the maximum vasodilation), constriction parameter a (this parameter has the units of mM and is the width of a Gaussian curve that controls how fast r drops as $[K^+]$ increases (Eq. 11)), and oxygen coupling constant γ . Duration is defined by the length of time that potassium concentration is elevated to a level greater than 6 mM. Increasing a , (shown from 30 – 80 mM) decreases the amount of constriction, resulting in quicker recovery from CSD. Likewise, increasing b , which increases the maximum dilation of the vessels, also reduces the duration of CSD.

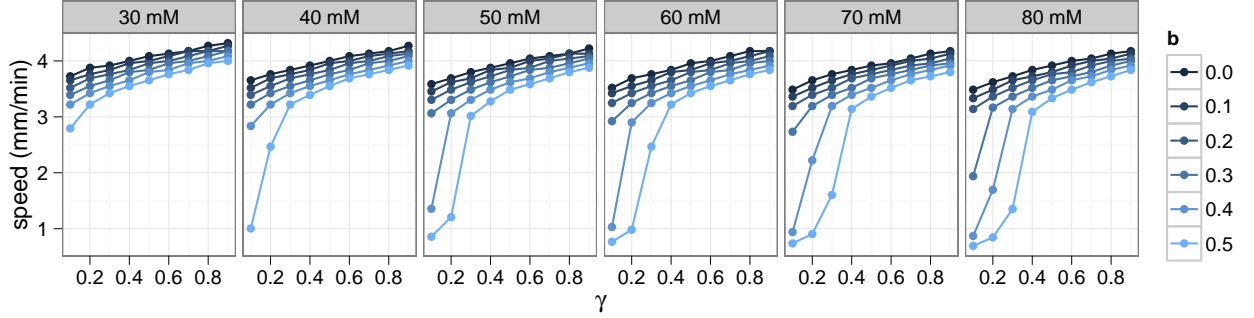


Figure 9. Speed of CSD for different vascular responses. Increasing the constriction parameter a makes the vessel less sensitive to potassium, weakening the resulting constriction. The speed decreases as a increases from 30 mM up to 80 mM, but increasing the amount of dilation by increasing b seems to have a greater effect.

4.2 Clinical and translational implications

If a major goal of CSD modeling is to understand its role in human disease, incorporation of perfusion and metabolism is an essential step. CSD is a near-maximal depolarization of brain tissue which of necessity challenges the ability of homeostatic mechanisms to compensate. CSD is also triggered by changes in perfusion or metabolism. Finally, during CSD, the relationships between brain activity, perfusion and metabolism - neurovascular coupling - are altered. These complex relationships can be expected to lead to a variety of responses, depending on the state of the brain tissue surrounding the depolarization. Biological data from animals and humans bears out this complexity and variability. Spreading depolarizations can be relatively innocuous - repetitive CSD in mouse over several days appears to cause

no overt injury [34]. However, they can also be quite harmful, enlarging infarct and contusion areas in both animals and humans [14, 35]. These deleterious effects are almost certainly due to alterations in the vascular response to tissue depolarization, and thus cannot be understood from a modeling standpoint without explicit incorporation of perfusion and metabolism.

Our model more realistically represents conditions observed in the brain during experimental CSD and the spreading depolarizations of migraine and brain injury. Though it simplifies a complex vascular/metabolic response, it has the distinct advantage of making specific, quantifiable predictions which can be used to generate hypotheses for further experimentation. A particular advantage is the ability to explore the whole “CSD/metabolic parameter space,” which is not possible in biological experiments. This modeling could have important implications for the study of CSD in migraine, as the conditions which could generate such a massive depolarization in an awake behaving person remain obscure.

4.3 Assumptions, limitations, and future directions

In this study, in order to make our model as widely applicable as possible, we have not considered the geometry of any particular vascular network. Our lumped model is assumed to be a good approximation of oxygen delivery dynamics in the brain, in general, for gray-matter. Further insight into the system may be gained by targeting specific tissue types for simulation.

Our simplified model relating arterial effective diameter to K^+ is likely applicable during CSD but does not mechanistically explain all the subtleties of neurovascular coupling under more normal conditions. Though K^+ is involved in the coupling of neural and astrocytic activity to blood flow [36], other mediators including arachidonic acid derivatives, purines, nitric oxide, and possibly neurotransmitters are involved as well [7, 23, 37]. For the purposes of CSD, however, with its supra-physiological swings in extracellular potassium, K^+ likely provides a good leading-order approximation of vascular behavior. Many of these other mediators also work via their effects on potassium channels [28].

Swelling of individual cells [17, 38, 39] and the tissue as a whole [10] appears to occur during CSD. Whether cell-swelling plays an important role in CSD is a controversial topic, as recent computational studies have cast some doubt on its impact [16, 40]. For this reason, we have omitted cell swelling from our model.

Finally, this model is not equipped to account for the complexity of the post-CSD state. Chang et al. [10] found that extracellular K^+ levels remained constant during a long-lasting hypoperfusion and depolarization that was found to follow CSD. As this phase may be clinically relevant, future modeling will focus on trying to understand the K^+ -independent mechanisms involved in the etiology of this period.

Acknowledgements

The authors would like to thank Tom Chou (UCLA Biomathematics and Mathematics) for his insightful comments during the model-building phase of this project and his support of JCC.

The work presented here is based on work and discussions held by the authors before, during, and after the American Institute of Mathematics (AIM) SQuaRE workshops on Modeling Cortical Spreading Depression held in Palo Alto, California in May 2010 and August 2011. We thank AIM for their financial support of the SQuaRE and special thanks go to Estelle Basor for her warm hospitality and ensuring a convenient and stimulating work environment.

The authors thank grant number T32GM008185 from the National Institute of General Medical Sciences and grant number 58386MA from the Army Research Office (JCC); the National Institutes of Health (NINDS NS059072 and NS070084) and the Department of Defense (CDMRP PR100060) (KCB); the Natural Sciences and Engineering Research Council of Canada and the Mathematics in Technology and Complex Systems (HH), the National Science Foundation through grant DMS-1022848 (RMM, HH, JJW), and the Research Grants Council of the Hong Kong Special Administrative Region, China (JJW).

References

1. Bures J, Buresova O, Krivanek J (1974) The mechanism and applications of leao's spreading depression of eeg activity. New York: Academic .
2. Kraig R, Kunkler P (2002) Spreading depression: a teleological means for self-protection from brain ischemia. In: Cerebrovascular Disease (22nd Princeton Research Conference). pp. 142–157.
3. Tfelt-Hansen P (2010) History of migraine with aura and cortical spreading depression from 1941 and onwards. *Cephalalgia* 30: 780–792.
4. Hadjikhani N, Sanchez del Rio M, Wu O, Schwartz D, Bakker D, et al. (2001) Mechanisms of migraine aura revealed by functional mri in human visual cortex. *Proceedings of the National Academy of Sciences* 98: 4687.
5. Lashley K (1941) Patterns of cerebral integration indicated by the scotomas of migraine. *Archives of Neurology and Psychiatry* 46: 331.
6. Leão A (1944) Spreading depression of activity in the cerebral cortex. *Journal of Neurophysiology* 7: 359.
7. Brennan K, Charles A (2010) An update on the blood vessel in migraine. *Current opinion in neurology* 23: 266.
8. Charles A, Brennan K (2009) Cortical spreading depressionnew insights and persistent questions. *Cephalalgia* 29: 1115–1124.
9. Busija D, Bari F, Domoki F, Horiguchi T, Shimizu K (2008) Mechanisms involved in the cerebrovascular dilator effects of cortical spreading depression. *Progress in neurobiology* 86: 417–433.
10. Chang J, Shook L, Biag J, Nguyen E, Toga A, et al. (2010) Biphasic direct current shift, haemoglobin desaturation and neurovascular uncoupling in cortical spreading depression. *Brain* 133: 996.
11. Piilgaard H, Lauritzen M (2009) Persistent increase in oxygen consumption and impaired neurovascular coupling after spreading depression in rat neocortex. *Journal of Cerebral Blood Flow & Metabolism* 29: 1517–1527.
12. Somjen G (2001) Mechanisms of spreading depression and hypoxic spreading depression-like depolarization. *Physiological reviews* 81: 1065–1096.
13. Lauritzen M, Dreier J, Fabricius M, Hartings J, Graf R, et al. (2010) Clinical relevance of cortical spreading depression in neurological disorders: migraine, malignant stroke, subarachnoid and intracranial hemorrhage, and traumatic brain injury. *Journal of Cerebral Blood Flow & Metabolism* 31: 17–35.
14. Dreier J (2011) The role of spreading depression, spreading depolarization and spreading ischemia in neurological disease. *Nature medicine* 17: 439–447.
15. Sukhotinsky I, Dilekoz E, Moskowitz M, Ayata C (2008) Hypoxia and hypotension transform the blood flow response to cortical spreading depression from hyperemia into hypoperfusion in the rat. *J Cerebral Blood Flow & Metabolism* 28: 1369–1376.
16. Yao W, Huang H, Miura R (2010) A continuum neuronal model for the instigation and propagation of cortical spreading depression. *Bulletin of Mathematical Biology* : 1–18.

17. Kager H, Wadman W, Somjen G (2000) Simulated seizures and spreading depression in a neuron model incorporating interstitial space and ion concentrations. *Journal of neurophysiology* 84: 495.
18. Kager H, Wadman W, Somjen G (2002) Conditions for the triggering of spreading depression studied with computer simulations. *Journal of neurophysiology* 88: 2700.
19. Keener J, Sneyd J (2009) *Mathematical physiology: cellular physiology*, volume 1. Springer Verlag.
20. Cloutier M, Bolger F, Lowry J, Wellstead P (2009) An integrative dynamic model of brain energy metabolism using in vivo neurochemical measurements. *Journal of computational neuroscience* 27: 391–414.
21. Klein J, Ergin M (2003) *Principles of cerebral protection during operations on the thoracic aorta. Advanced Therapy in Cardiac Surgery* Hamilton, Canada: BC Decker Inc : 291–303.
22. Chih C, Roberts E (2003) Energy substrates for neurons during neural activity; a critical review of the astrocyte-neuron lactate shuttle hypothesis. *Journal of Cerebral Blood Flow & Metabolism* 23: 1263–1281.
23. Attwell D, Buchan A, Charkpak S, Lauritzen M, MacVicar B, et al. (2010) Glial and neuronal control of brain blood flow. *Nature* 468: 232–243.
24. Somjen G (1975) Electrophysiology of neuroglia. *Annual review of physiology* 37: 163–190.
25. Zamir M. *The physics of pulsatile flow*. 2000.
26. Knot H, Zimmermann P, Nelson M (1996) Extracellular K^+ -induced hyperpolarizations and dilatations of rat coronary and cerebral arteries involve inward rectifier K^+ channels. *The Journal of physiology* 492: 419.
27. McCarron J, Halpern W (1990) Potassium dilates rat cerebral arteries by two independent mechanisms. *American Journal of Physiology-Heart and Circulatory Physiology* 259: H902–H908.
28. Farr H, David T (2011) Models of neurovascular coupling via potassium and eet signalling. *Journal of Theoretical Biology* .
29. Laughlin S, van Steveninck R, Anderson J (1998) The metabolic cost of neural information. *Nature neuroscience* 1: 36–41.
30. Aperia A (2001) Regulation of sodium/potassium atpase activity: impact on salt balance and vascular contractility. *Current hypertension reports* 3: 165–171.
31. Heinemann U, Dieter Lux H (1977) Ceiling of stimulus induced rises in extracellular potassium concentration in the cerebral cortex of cat. *Brain research* 120: 231–249.
32. Takano T, Tian G, Peng W, Lou N, Lovatt D, et al. (2007) Cortical spreading depression causes and coincides with tissue hypoxia. *Nature neuroscience* 10: 754–762.
33. Sakadžić S, Yuan S, Dilekoz E, Ruvinskaya S, Vinogradov S, et al. (2009) Simultaneous imaging of cerebral partial pressure of oxygen and blood flow during functional activation and cortical spreading depression. *Applied optics* 48: D169–D177.
34. Sukhotinsky I, Dilekoz E, Wang Y, Qin T, Eikermann-Haerter K, et al. (2011) Chronic daily cortical spreading depressions suppress spreading depression susceptibility. *Cephalalgia* 31: 1601–1608.

35. Dreier J, Major S, Manning A, Woitzik J, Drenckhahn C, et al. (2009) Cortical spreading ischaemia is a novel process involved in ischaemic damage in patients with aneurysmal subarachnoid haemorrhage. *Brain* 132: 1866–1881.
36. Filosa J, Bonev A, Nelson M (2004) Calcium dynamics in cortical astrocytes and arterioles during neurovascular coupling. *Circulation research* 95: e73–e81.
37. Gordon G, Choi H, Rungta R, Ellis-Davies G, MacVicar B (2008) Brain metabolism dictates the polarity of astrocyte control over arterioles. *Nature* 456: 745–749.
38. Mazel T, Richter F, Vargová L, Syková E (2002) Changes in extracellular space volume and geometry induced by cortical spreading depression in immature and adult rats. *Physiol Res* 51: 85–94.
39. Shapiro B (2001) Osmotic forces and gap junctions in spreading depression: a computational model. *Journal of Computational Neuroscience* 10: 99–120.
40. Bennett M, Farnell L, Gibson W (2008) A quantitative model of cortical spreading depression due to purinergic and gap-junction transmission in astrocyte networks. *Biophysical journal* 95: 5648–5660.

A Cross-Membrane Currents and Parameter Values

We assume that the membrane currents in the soma used by Kager et al. [17] apply here. The total cross-membrane current in the soma is given by the sum of the active and passive sodium, potassium, chloride, and nonspecific ionic currents. The sodium current is $I_{s,Na,tot} = I_{s,Na,P} + I_{s,Na,Leak} + I_{s,Na,Pump}$ where $I_{Na,P}$ is the persistent sodium current, $I_{s,Na,leak}$ is the sodium leak current, and $I_{s,Na,pump}$ is the current through the pump. The active and passive potassium currents are $I_{s,K,tot} = I_{s,K,DR} + I_{s,K,A} + I_{s,K,leak} + I_{s,K,pump}$ where $I_{s,K,DR}$ is the potassium delayed rectifier current, $I_{s,K,A}$ is the transient potassium current, $I_{s,K,pump}$ is the potassium current through the pump, and $I_{s,K,leak}$ is the potassium leak current. The passive chloride leak current is $I_{s,leak}$.

In the dendritic compartment, the NMDA currents, $I_{d,Na,NMDA}$ and $I_{d,K,NMDA}$, are added to the total current. Note that we have removed $I_{s,Na,T}$, the fast transient sodium current, since this current was shown in [16] to not make any fundamental difference in the way CSD propagates. The mathematical expressions for these channels do not differ across the dendritic and somatic compartments so we omit the compartment prefix (s, d) from this point forward.

The cross-membrane currents are modeled using: *i*) the Goldman-Hodgkin-Katz (GHK) formulas for the active membrane currents given by

$$I_{ion,GHK} = m^p h^q \frac{g_{ion,GHK} F E_m \left[[ion]_i - \exp\left(-\frac{E_m}{\phi}\right) [ion]_e \right]}{\phi \left[1 - \exp\left(-\frac{E_m}{\phi}\right) \right]}, \quad (14)$$

which is suitable when there is a large difference in concentrations between the ICS and ECS compartments, as argued by Koch and Segev [19] and *ii*) the Hodgkin-Huxley (HH) model for the passive leak currents given by

$$I_{ion,HH} = g_{ion,HH} (E_m - E_{ion}). \quad (15)$$

In these general expressions for the GHK and HH types of currents, $g_{ion,GHK}$ and $g_{ion,HH}$ are the conductances associated with the channels for ion = Na⁺ and K⁺, and m and h are the activation and inactivation gating variables, respectively, for the different GHK-modeled channels that are ion-specific. Note that the $g_{ion,HH}$ conductances for the sodium and potassium leak currents and the g_{leak} conductance for the chloride leak current are assumed to be constant. The variables, E_{ion} , are the Nernst potentials for ion = Na⁺ and K⁺ given by

$$E_{ion} = \phi \log \frac{[ion]_e}{[ion]_i}. \quad (16)$$

For the chloride leak current, the equivalent Nernst potential is -70mV . The factors in the parameter $\phi = RT/F$ are R , the universal gas constant, $T = 310\text{K}$, the absolute temperature, and F , the Faraday constant.

The gating variables, m and h , satisfy the following relaxation equations

$$\frac{dm}{dt} = \alpha_m(1 - m) - \beta_m m, \quad (17)$$

$$\frac{dh}{dt} = \alpha_h(1 - h) - \beta_h h, \quad (18)$$

and the values of α and β are given in Table 1, along with the exponents p and q [18]. The extracellular volume is assumed to be 15% of the intracellular volume, i.e., $V_e = 0.15V_i$. Other relevant parameter values are: $R = 8.31$ (mV coulomb/mM K) and $F = 96.485$ coulomb/mM.

We use the following procedure to choose the initial (equilibrium) values for the gating variables and ion concentrations. We first set the membrane potential at $E_m = -70$ mV and the sodium and potassium concentrations (listed in Table 2), from which we compute the parameters α and β (using the formulas in Table 1). We then compute the equilibrium values of m and h as

$$m = \frac{\alpha_m}{\alpha_m + \beta_m}, \quad h = \frac{\alpha_h}{\alpha_h + \beta_h}.$$

Next we choose the leak conductances, $g_{\text{Na,leak}}$ and $g_{\text{K,leak}}$, by setting

$$I_{\text{Na,tot}} = I_{\text{K,tot}} = 0.$$

Finally, we determine the chloride leak conductance in I_{leak} by assuming that $g_{\text{leak}} = 10g_{\text{Na,leak}}$.

Table 1. Parameter values for active membrane ionic currents, from [17, 18].

Currents mA/cm ²	$g_{\text{ion,GHK}}$ S/cm ²	Gates $m^p h^q$	Voltage-Dependent Rate Constants
$I_{\text{Na,P}}$	2×10^{-6}	$m^2 h$	$\alpha_m = \frac{1}{6(1 + \exp[-(0.143E_m \text{mV}^{-1} + 5.67)])}$ $\beta_m = \frac{\exp[-(0.143E_m \text{mV}^{-1} + 5.67)]}{6(1 + \exp[-(0.143E_m \text{mV}^{-1} + 5.67)])}$ $\alpha_h = 5.12 \times 10^{-8} \exp[-(0.056E_m \text{mV}^{-1} + 2.94)]$ $\beta_h = \frac{1.6 \times 10^{-6}}{1 + \exp[-(0.2E_m \text{mV}^{-1} + 8)]}$
$I_{\text{K,DR}}$	10×10^{-5}	m^2	$\alpha_m = 0.016 \frac{E_m \text{mV}^{-1} + 34.9}{1 - \exp[-(0.2E_m \text{mV}^{-1} + 6.98)]}$ $\beta_m = 0.25 \exp[-(0.25E_m \text{mV}^{-1} + 1.25)]$
$I_{\text{K,A}}$	1×10^{-5}	$m^2 h$	$\alpha_m = 0.02 \frac{E_m \text{mV}^{-1} + 56.9}{1 - \exp[-(0.1E_m \text{mV}^{-1} + 5.69)]}$ $\beta_m = 0.0175 \frac{E_m \text{mV}^{-1} + 29.9}{\exp(0.1E_m \text{mV}^{-1} + 2.99) - 1}$ $\alpha_h = 0.016 \exp[-(0.056E_m \text{mV}^{-1} + 4.61)]$ $\beta_h = \frac{0.5}{1 + \exp[-(0.2E_m \text{mV}^{-1} + 11.98)]}$
I_{NMDA}	1×10^{-5}	mh	$\alpha_m = \frac{0.5}{1 + \exp\left(\frac{13.5 - [\text{K}^+]_e \text{mM}^{-1}}{1.42}\right)}$ $\beta_m = 0.5 - \alpha_m$ $\alpha_h = \frac{1}{2000(1 + \exp\left[\frac{[\text{K}^+]_e \text{mM}^{-1} - 6.75}{0.71}\right])}$ $\beta_h = 5 \times 10^{-5} - \alpha_h$

The initial resting ion concentrations consistent with those in [17, 18] are obtained by modifying the sodium-potassium exchange pump function and running the model equations until a steady state is reached. These values are given in Table 2 together with other parameter values.

Table 2. Initial resting values and other relevant parameter values for the computations, following Kager et al. [17,18].

Parameter	Value	Unit
R_a (input resistance of dendritic tree)	1.83×10^5	ohms
d_s (diameter of soma)	5.45×10^{-4}	cm
d_d (diameter of dendrite)	0.939×10^{-4}	cm
δ_d (half-length of dendrite)	4.5×10^{-2}	cm
A_s (surface area of soma)	1586×10^{-8}	cm ²
A_d (surface area of dendrite)	26732×10^{-8}	cm ²
V_s (volume of soma)	2160×10^{-12}	cm ³
V_d (volume of dendrite)	5614×10^{-12}	cm ³
C_m (membrane capacitance)	7.5×10^{-5}	s / Ω cm ²
I_{max} (Na ⁺ /K ⁺ -ATPase rate)	1.48×10^{-3}	mA / cm ²
E_m	-70	mV
$[K^+]_e$	3.5	mM
$[K^+]_i$	133.5	mM
$[Na^+]_e$	140	mM
$[Na^+]_i$	10	mM
$[O_2]_0$	2×10^{-2}	mM
CBF_0	2.5×10^{-2}	mM/s
D_{O_2}	0.5×10^{-5}	cm ² /s
$[O_2]_b$	4×10^{-2}	mM